

Thermodynamic and electronic properties of rutile $\text{Sn}_{1-x}\text{Ge}_x\text{O}_2$ alloys from first principles

Yann L. Müller,^{1,*} Alp Umut Kurbay,^{2,*} Xiao Zhang,² Emmanouil Kioupakis,^{2,†} and Anirudh Raju Natarajan^{1,3,‡}

¹*Laboratory of materials design and simulation (MADES),
Institute of Materials, École Polytechnique Fédérale de Lausanne*

²*Department of Materials Science and Engineering, University of Michigan, Ann Arbor, Michigan 48109, USA*

³*National Centre for Computational Design and Discovery of Novel Materials (MARVEL), École Polytechnique Fédérale de Lausanne*

Rutile $\text{Sn}_{1-x}\text{Ge}_x\text{O}_2$ alloys are promising materials for high-power electronic applications due to their dopability and tunable ultra-wide band gaps. We use first-principles density functional theory and statistical mechanics to investigate the crystallographic, electronic, and thermodynamic properties of rutile $\text{Sn}_{1-x}\text{Ge}_x\text{O}_2$ alloys. We predict that the lattice parameters follow Vegard's law, while band gaps calculated with the hybrid HSE06 functional exhibit strong bowing, consistent with experiment. We also predict that the disordered phase has a large positive mixing enthalpy and a slight tendency for Ge-Sn clustering, indicated by weakly negative short-range order parameters. This large positive mixing enthalpy produces a miscibility gap with a critical temperature above 2300 K, implying that the high Ge and Sn solubilities observed in thin-film synthesis cannot be explained by the incoherent phase diagram alone. We demonstrate that coherency strain during epitaxial growth substantially alters phase stability. Calculations of the coherent spinodal show significant suppression of the miscibility gap, reducing the critical temperature to ≈ 900 K. These coherent phase boundaries account for the experimentally observed high solubilities at typical growth temperatures. Our results indicate that coherency strain stabilizes these metastable alloys and enables bandgap engineering in this ultrawide-bandgap material system.

Semiconductors with band gaps wider than that of GaN (3.4 eV), known as ultra-wide-band-gap (UWBG) semiconductors, are promising for high-power electronic devices and UV-visible optoelectronics[1]. UWBG materials can tolerate higher electric fields than conventional semiconductors due to the superlinear increase of the critical dielectric breakdown field with increasing band gap. Several UWBG materials are under investigation [1], including diamond, cubic boron nitride, aluminum-gallium-nitride alloys, and semiconducting oxides such as β - Ga_2O_3 , SnO_2 , rutile GeO_2 , and rutile SiO_2 [2, 3].

Rutile GeO_2 (r- GeO_2) and its alloys with SnO_2 , in particular, have recently emerged as promising materials for UWBG applications due to their attractive electronic properties. r- GeO_2 has been predicted to exhibit an ultra-wide band gap of 4.68 eV [4], efficient n-type (and potential ambipolar) doping [5], high electron and hole mobilities[6] and high thermal conductivity [7]. The large band gap and high carrier mobilities of r- GeO_2 yield a high Baliga's figure of merit[8] surpassing other power electronic candidates such as Ga_2O_3 . The n-type dopability has been experimentally demonstrated for bulk [9] and thin-film [10] samples, while MOSFET devices [11] and vertical Schottky barrier diodes [12] based on r- GeO_2 have recently been demonstrated.

Alloying r- GeO_2 with r- SnO_2 yields a tunable band gap ranging from 4.68 eV (r- GeO_2) to 3.6 eV (r- SnO_2). Pulsed laser deposition[13, 14], chemical vapor deposition[15], sputtering[16, 17], and molecular beam epitaxy[18, 19] have been utilized to synthesize rutile $\text{Sn}_{1-x}\text{Ge}_x\text{O}_2$ (r- $\text{Sn}_{1-x}\text{Ge}_x\text{O}_2$). However, film quality is sensitive to the composition, often suffering from amorphization and challenges

in obtaining single-phase as the Ge content increases.

In this study, we systematically investigate the thermodynamic and electronic properties of r- $\text{Sn}_{1-x}\text{Ge}_x\text{O}_2$ alloys using density functional theory (DFT) and statistical mechanics-based calculations. Our results reveal that the lattice parameters of disordered solid solutions follow Vegard's law, and the band gaps exhibit a bowing effect. Finite-temperature thermodynamic calculations, based on both an approximate free-energy model and more accurate Monte-Carlo simulations informed by on-lattice cluster expansions, predict a high-temperature miscibility gap consistent with early experiments. Finally, we show that the variation in solid solubilities observed across synthesis techniques likely stems from the suppression of the miscibility gap due to coherency strain. Our results highlight the importance of accounting for coherency strain effects on phase stability in alloys of r- GeO_2 .

Density functional theory (DFT) calculations with the Perdew-Burke-Ernzerhof (PBE)[20], r²SCAN[21], and HSE06[22] functionals were used to study the crystallographic, thermodynamic and electronic properties of r- $\text{Sn}_{1-x}\text{Ge}_x\text{O}_2$. We employed HSE06 hybrid-functional calculations, in particular, to obtain accurate band gaps, as the other two functionals systematically underestimate them. All DFT calculations used projector augmented-wave (PAW) potentials as implemented in the Vienna *Ab Initio* Simulation Package (VASP)[23, 24]. We relaxed structures with the PBE[20] and r²SCAN functionals until forces on atoms converged to less than 0.01 eV/Å. These calculations treated Ge $4s^23d^{10}4p^2$ and Sn $5s^24d^{10}5p^2$ as valence electrons, with a plane-wave energy cutoff of 600 eV and a Γ -centered k-point grid density of 35Å. For HSE06 calculations, we used GW-compatible PBE pseudopotentials with a mixing parameter of 0.315 for all compositions. The HSE06 calculations included the Ge $3s^23p^6$ and Sn $4s^24p^6$ electrons in addition to those above, with a plane-wave energy cutoff of 950 eV to

* These authors contributed equally to this work.

† kioup@umich.edu

‡ anirudh.natarajan@epfl.ch

ensure total energy convergence within 0.1 meV/atom. We sampled the Brillouin zone with a Γ -centered $4 \times 4 \times 6$ grid for binary unit cells and a Γ -centered $2 \times 2 \times 2$ grid for alloy supercells.

The rutile structure, shown in fig. 1a), accommodates disorder on the cation sublattice, where each site can be occupied by either Ge or Sn atoms. We do not consider disorder on the anion (oxygen) sublattice. We approximate properties of the disordered phase using special quasi-random structures (SQS)[25]. SQS-based chemical orderings were generated in a simulation cell containing 72 atoms (24 formula units) for seven equally spaced compositions ranging from pure SnO_2 ($x = 0$) to GeO_2 ($x = 1$), ensuring that pair cluster functions were disordered up to the sixth nearest neighbor shell. We re-

laxed structures with respect to lattice parameters and atomic positions using the PBE, $r^2\text{SCAN}$, and HSE06 functionals to obtain lattice parameters and total energies. The band gaps of the SQS structures were calculated with the HSE06 functional.

Understanding the finite-temperature synthesizability of disordered $\text{r-Sn}_{1-x}\text{Ge}_x\text{O}_2$ alloys requires quantifying the thermodynamics of the binary alloy. Finite-temperature free energies can be estimated through several methods. The simplest approximation uses the energies of SQS structures to construct a free energy model. The formation energy (Δe_f) for a specific arrangement of Ge and Sn on the rutile lattice is given by

$$\Delta e_f(\text{Sn}_{2(1-x)}\text{Ge}_{2x}\text{O}_4) = \frac{2}{M} (E(\text{Sn}_{(M-N)}\text{Ge}_N\text{O}_{2M}) - NE(\text{GeO}_2) - (M-N)E(\text{SnO}_2)) \quad (1)$$

where $E(\text{Sn}_{(M-N)}\text{Ge}_N\text{O}_{2M})$ is the total energy of a supercell containing M total cation sites. N of these sites are occupied by Ge (giving a composition $x = N/M$). $E(\text{GeO}_2)$ and $E(\text{SnO}_2)$ are the total energies per formula unit of bulk rutile GeO_2 and SnO_2 , respectively. Equation (1) is the formation energy per rutile primitive cell containing two formula units of $\text{r-Sn}_{1-x}\text{Ge}_x\text{O}_2$. The formation energies of the SQS structures are used to fit the mixing enthalpy (Δh_{dis}) of the disordered solid solution with a subregular solution model

$$\Delta h_{dis}(\text{Sn}_{2(1-x)}\text{Ge}_{2x}\text{O}_4) = \alpha x(1-x) + \beta x(1-x)(1-2x) \quad (2)$$

where α and β are parameters fitted to the DFT-computed SQS formation energies. The ideal mixing entropy (Δs_{mix}) per primitive cell is estimated as

$$\Delta s_{dis}(\text{Sn}_{2(1-x)}\text{Ge}_{2x}\text{O}_4) = -2k_B(x \ln(x) + (1-x) \ln(1-x)) \quad (3)$$

where the factor of 2 arises from the two cation sites within the rutile primitive unit cell. The free energy of the disordered phase is computed as $\Delta g_{\text{disordered}}(\text{Sn}_{2(1-x)}\text{Ge}_{2x}\text{O}_4, T) = \Delta h_{dis} - T\Delta s_{dis}$.

The approximate free energy model constructed with the formation energies of the SQS structures and ideal solution mixing entropy does not account for the formation of any ordered phases or the formation of short-range order within the disordered solid solution. A more accurate estimate of finite-temperature thermodynamics in systems with order-disorder transitions can be obtained from statistical mechanics simulations. These simulations are informed by surrogate models, such as on-lattice cluster expansions (CE), which are parameterized using DFT calculations for a small set of symmetrically distinct arrangements on a parent crystal structure. Cluster expansion Hamiltonians[26, 27] are effective tools for assessing the thermodynamic properties of crystalline materials[28–38]. Within the cluster expansion formalism, any arrangement of Sn and Ge on the rutile lattice is represented by an occupation vector $\vec{\sigma} = [\sigma_1 \ \sigma_2 \ \dots \ \sigma_N]^T$.

The i th entry σ_i takes the value -1 if the i th lattice site is occupied by Sn and 1 if occupied by Ge. The formation energy $\Delta e_f(\vec{\sigma})$ of an arbitrary arrangement $\vec{\sigma}$ in this alloy is given by:

$$\Delta e_f(\vec{\sigma}) = \frac{1}{M} \left(V_0 + \sum_i V_i \sigma_i + \sum_{i,j} V_{ij} \sigma_i \sigma_j + \dots \right) \quad (4)$$

where V_0 , V_i , and V_{ij} are fitting coefficients known as effective cluster interactions (ECI). The CE is then used within Monte-Carlo simulations and free-energy integration methods to compute the finite-temperature free energy of all relevant phases in the alloy. Common tangent constructions are then employed to compute phase boundaries.

Figure 1 shows the calculated lattice constants and band gap of $\text{r-Sn}_{1-x}\text{Ge}_x\text{O}_2$ alloys as a function of alloy composition x . Figure 1b shows the calculated PBE, $r^2\text{SCAN}$, and HSE lattice constants averaged over three SQS supercells containing 72 atoms. The HSE and $r^2\text{SCAN}$ results are in excellent agreement with experimental studies, whereas PBE overestimates the lattice constants due to the well-known underbinding tendency of the functional. The calculated lattice constants clearly demonstrate the validity of Vegard’s law in all three cases.

The bandgaps for the SQS structures computed with the HSE06 hybrid functional are shown in fig. 1b. Bandgaps are averaged over three different SQSs at each composition. We find a direct bandgap at the Γ point across all compositions, which is fit to a second-order composition-dependent bowing model:

$$E_g(x) = xE_{g,\text{GeO}_2} + (1-x)E_{g,\text{SnO}_2} - x(1-x)[bx + c(1-x)] \quad (5)$$

The second-order bowing fit is employed here to more effectively capture variations of the bowing parameter with respect to composition, as observed in other UWBG semiconductor alloys such as $\text{Al}_{1-x}\text{In}_x\text{N}$ [39]. This fit yields bowing

	α (eV/unit cell)	β (eV/unit cell)
Δh_{dis} (PBE)	0.915	-0.117
Δh_{dis} (r ² SCAN)	1.071	-0.219

TABLE I. Fitting parameters for the subregular solution model of the disordered phase enthalpy, based on eq. (2).

parameters $b = 1.115 \pm 0.01$ eV and $c = 1.336 \pm 0.005$ eV, indicating stronger bowing at lower Ge content. Both of these values are in agreement with experimental results reported by Takane *et al.*, who found a bowing parameter of 1.2 eV using a first-order fit [15]. It should be noted that while our calculated bandgap of 3.6 eV for SnO_2 agrees with experimental studies of the bulk material, this value is roughly 200 meV lower than that reported in experimental optical absorption measurements for thin-film samples [13, 15]. This discrepancy may arise from the dipole-allowed or -forbidden nature of the transitions depending on symmetry breaking due to alloy disorder, or from strain effects in the thin-film samples used experimentally.

Figure 2 compares the 0 K and finite-temperature phase stability of $\text{r-Sn}_{1-x}\text{Ge}_x\text{O}_2$ alloys as computed with different exchange-correlation functionals. The formation energies of the 21 SQS orderings, shown in fig. 2a, are qualitatively similar when computed with PBE and r²SCAN. However, the r²SCAN values are up to 17% higher than the PBE values, a difference that is largest at high germanium compositions. Both DFT functionals predict positive mixing enthalpies. This result indicates low-temperature phase separation and suggests that mixing between the terminal oxides occurs only at higher temperatures. We used the SQS formation energies of fig. 2a to fit the subregular solution model for the disordered phase enthalpy (eq. (2)). The resulting fitting parameters are listed in table I. The large positive values of α in table I indicate significant immiscibility in this alloy.

Figure 2b shows the finite-temperature phase diagrams computed with the PBE and r²SCAN functionals using the SQS-based free energy model. Both phase diagrams predict a wide miscibility gap, indicating phase separation. For an equiatomic solid solution, the critical temperature is predicted to be ~ 2750 K with PBE and ~ 3350 K with r²SCAN. The higher critical temperature from r²SCAN is a direct result of the larger SQS formation energies predicted by that functional. These results are in qualitative agreement with the experimental phase diagram reported by Watanabe *et al.* [42]. Their work suggests $\approx 4\%$ solubility of GeO_2 in SnO_2 at 1250 °C, with very little solubility of SnO_2 in GeO_2 . Our calculations show a similar trend, predicting low solubility of GeO_2 in SnO_2 and minimal dissolution at the GeO_2 -rich end of the phase diagram.

The SQS-based approximate free energy model provides finite-temperature predictions consistent with experiment, but quantitative differences in phase stability can arise from short or long-range ordering effects. A rigorous evaluation of finite-temperature phase stability was performed using the CE method. We computed the formation energies of all 80 symmetrically distinct chemical decorations of Ge and Sn on

the rutile cation sublattice within supercells containing up to 6 cation sites using the PBE functional. The computed formation energies are shown in fig. 2c. No ordered ground states are predicted to be stable at 0 K. The positive formation energies suggest immiscibility at low temperatures, in agreement with the formation energies of the SQS orderings in fig. 2a. To parameterize the CE model based on these 80 formation energies, descriptors of chemical ordering were computed with the *Clusters Approach to Statistical Mechanics (CASM)* software package [43–45] for clusters containing up to 4 sites located within a maximum distance of 9 Å. A 5-fold cross-validated Lasso model [46], as implemented in the `sklearn` package [47], was utilized for the linear regression. The resulting CE model achieved a root mean squared error (RMSE) of 9 meV/unit cell (1.5 meV/atom). A comparison between the DFT and CE formation energies is shown in fig. 2c.

Figure 2b compares the finite-temperature phase diagram for $\text{r-Sn}_{1-x}\text{Ge}_x\text{O}_2$ derived from rigorous CE-based statistical mechanics with the prediction from the SQS-based approximate free energy model. The CE-based phase boundaries were determined using semi-grand canonical Monte Carlo simulations, followed by free energy integration and a common tangent construction. The resulting miscibility gap is shown by the black dots in fig. 2b (left). The critical temperature predicted by the CE model is approximately 400 K lower than that predicted by the PBE-based subregular model.

Small discrepancies between the phase boundaries predicted by the CE and SQS-based models arise from differences in the mixing enthalpy and short-range order (SRO) effects. Figure 2c compares the CE-predicted enthalpy of the disordered solid solution to the SQS-informed subregular solution enthalpy. The CE mixing enthalpy is approximately 7% lower than the SQS-based PBE value. This enthalpy difference alone accounts for a ≈ 100 K reduction in the predicted critical temperature.

The remaining discrepancy arises from SRO near the phase transition. SRO formation lowers both the enthalpy and entropy of the disordered state compared to a perfectly random solution. When the enthalpy gain offsets the entropy penalty, the free energy of the disordered state decreases relative to the perfectly disordered random solution. Figure 3 displays the SRO of Ge-Sn pairs in the first, second, and third nearest-neighbor shells obtained from Monte Carlo simulations at 2400 K and 3000 K. A negative SRO parameter indicates more Ge-Sn pairs relative to a random alloy, while a positive value signifies fewer pairs. Figure 3 reveals a slight tendency for the clustering of Ge-Sn pairs in the first-nearest-neighbor shell (vertical edges in fig. 1a). An elevated number of Ge-Ge and Sn-Sn pairs are predicted to occur in the second and third nearest-neighbor shells. The degree of SRO is small, with absolute values remaining below 0.15. Figure 3 shows that SRO becomes more positive as the temperature decreases. This is consistent with a phase-separating behavior at low temperatures. The emergence of SRO near the phase transition likely accounts for the lower critical temperature predicted by the CE method relative to the approximate free energy model. The similarities in PBE and r²SCAN formation ener-

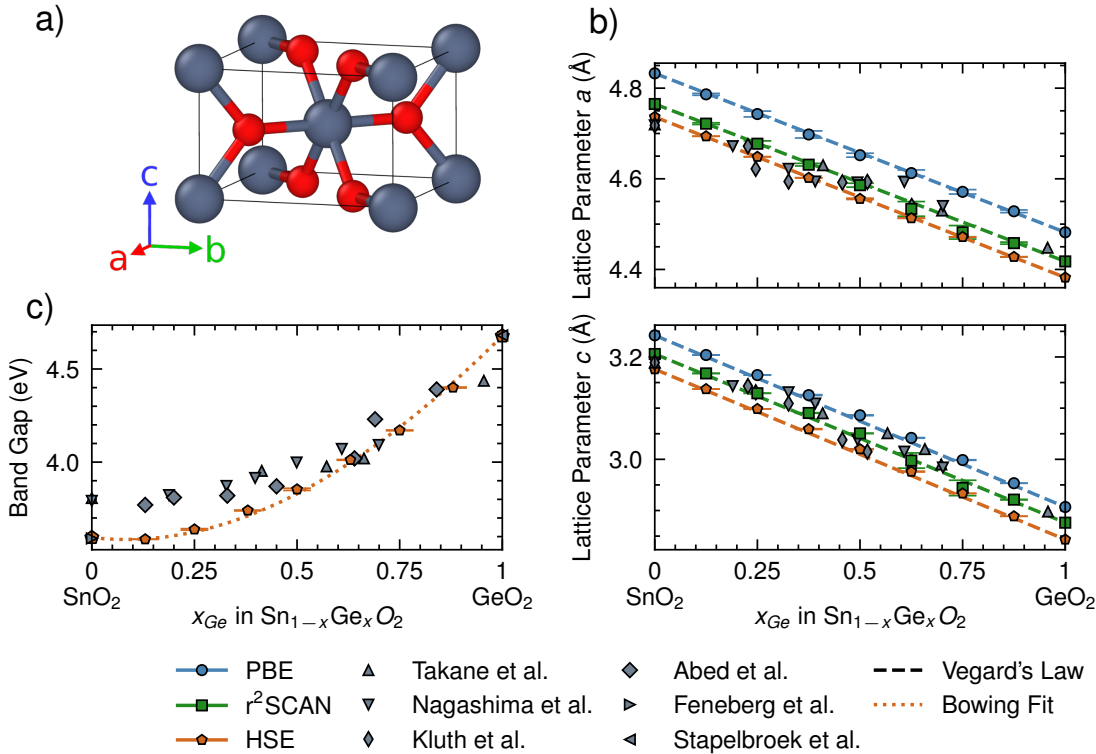


FIG. 1. a) Unit cell of the rutile structure. The blue atoms correspond to cation sites occupied by Ge or Sn atoms, while red sites correspond to oxygen atoms. b) Calculated PBE (blue circles), r^2 SCAN (green squares), HSE (orange pentagons) lattice constants a (top) and c (bottom), for $Sn_{1-x}Ge_xO_2$ alloys at $x = 0, 0.125, 0.25, 0.375, 0.5, 0.625, 0.75, 0.875, 1$. The values for the alloys are calculated by averaging three SQS supercells, each containing 72 atoms (a $2 \times 2 \times 3$ supercell of the primitive unit cell). The error bars represent the standard deviation. c) Calculated HSE bandgaps (orange pentagons) for $Sn_{1-x}Ge_xO_2$ alloys using 72 atom SQSs. The bowing fit is determined using a second-order composition-dependent model. The experimental data for alloy thin films are given by [15] (upward triangles), [13] (downward triangles), [17] (diamonds), and [14] (rhombuses), while the data for the bulk crystals is given by [40] (rightward triangles) and [41] (leftward triangles).

gies suggest that a similar discrepancy would emerge if the CE method were applied to the r^2 SCAN data. Nevertheless, the overall analysis presented in fig. 2 indicates a critical temperature for the disordered solid solution of $\approx 2350 - 2750$ K (PBE) or ≈ 3350 K (r^2 SCAN).

Our finite-temperature phase diagrams agree well with early experiments for bulk materials[42]. However, they appear to contradict recent reports of wide-ranging miscibility in thin films[15, 19] and a recent computational prediction[19]. On the computational side, the critical temperature predicted by our thermodynamic model is approximately 3 times higher than the calculated value of ≈ 986 K reported by Liu *et al.*[19]. This discrepancy exists despite the use of identical DFT functionals in both studies. The difference likely stems from the mixing enthalpy reported by Liu *et al.*[19], which is three times lower than our calculated values (table I). The significant difference in free energies leads to qualitatively different behavior. Liu *et al.* attribute their ability to grow films with 34% Ge in SnO_2 at 600 °C to the metastable solubility limit predicted by their calculated spinodal. In contrast, the spinodal predicted by our models (shown by the blue curves in fig. 2) indicates a metastable solubility limit of only $\approx 10\%$ at 600 °C. The observed higher

solubility of Ge in SnO_2 is unlikely to be explained solely by the incoherent spinodal decomposition and miscibility gap shown in fig. 2.

The phase diagrams in fig. 2 represent incoherent equilibria, showing phase boundaries and solubility limits for phases that form without microstructural constraints. In epitaxially grown thin films, incoherent equilibria are often not achieved. Instead, constraints imposed by the growth conditions force coexisting phases to share the same lattice parameters, leading to coherent phase coexistence. Coherent phase diagrams are known to differ quantitatively from their incoherent counterparts. This coherency can significantly alter solubility limits and phase stability in materials classes ranging from metallic alloys[48] to thermoelectric[49] and battery materials[50].

Precisely estimating coherent phase equilibrium is challenging as phase compositions are sensitive to microstructure, local stresses, and composition-dependent material properties. Qualitative estimates, however, can be obtained using approximations introduced by Cahn[51] and implemented by Doak and Wolverton[49]. Within this framework, the enthalpy of the disordered phase under the constraint of

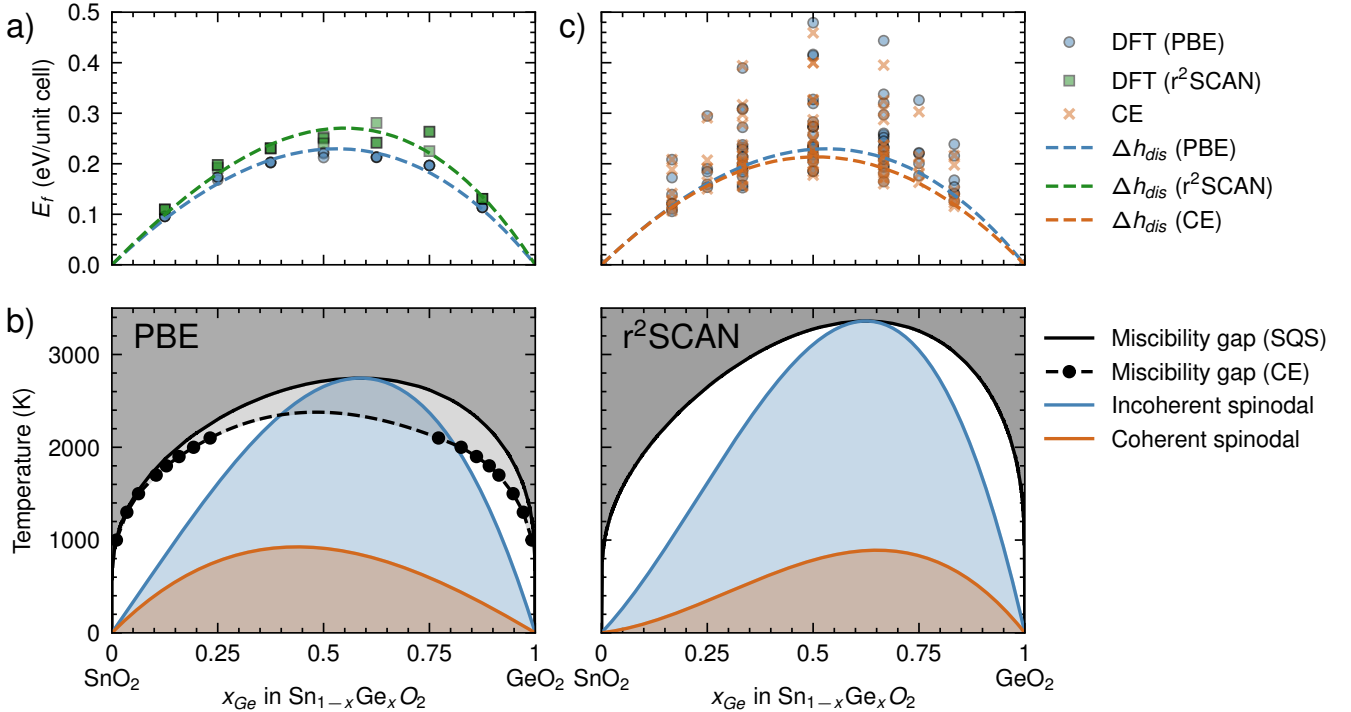


FIG. 2. a) DFT formation energies of the SQS structures evaluated with PBE (blue circles) and r^2 SCAN (green squares) functionals. The dashed lines represent the enthalpy of the disordered phase estimated with the subregular solution model. b) Phase diagrams of the r - $Sn_{1-x}Ge_xO_2$ computed using PBE functional (left) and r^2 SCAN functional (right). The black solid line indicates the miscibility gap, the blue line the incoherent spinodal, and the orange line the coherent spinodal along the [001] direction. The miscibility gap obtained through free energy integration using the CE is indicated by black dots in the PBE phase diagram. c) Convex hull computed with 80 symmetrically distinct orderings on r - $Sn_{1-x}Ge_xO_2$ predicted by DFT (blue circles) and CE (orange crosses), using the PBE functional. The blue dashed lines are the disordered enthalpy estimated with the subregular solution model fit to the DFT formation energies of the SQS structures. The orange dashed line is the enthalpy of a perfectly disordered solid solution estimated with the CE model.

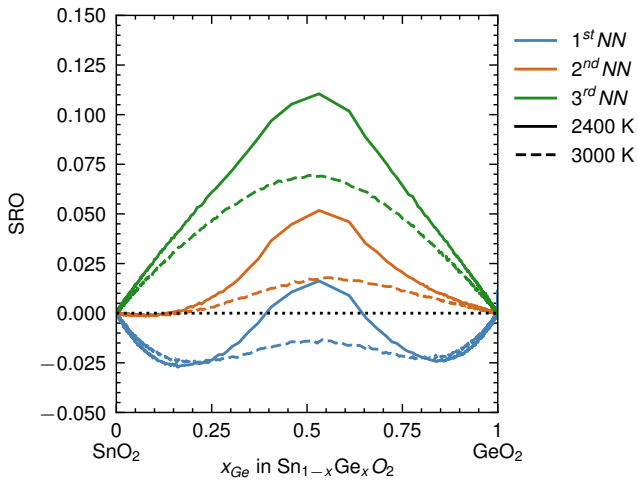


FIG. 3. Plot of the Ge-Sn SRO as a function of the composition for the first (blue), second (orange), and third (green) nearest-neighbor shells, computed at 2400 K (solid line) and at 3000 K (dashed line).

coherent equilibrium is:

$$\Delta h_{dis}^{coh}(x) = \Delta h_{dis}(x) - \Delta e_{cs}(x) \quad (6)$$

where Δh_{dis} is the incoherent enthalpy of the disordered state (eq. (2)) and Δe_{cs} is the coherency strain energy due to phase coexistence at the same lattice parameters. As described by Doak and Wolverton[49], an approximate coherency strain energy can be computed along different coexistence planes. This calculation involves fixing the in-plane lattice parameters of the terminal oxides and minimizing the energy with respect to the out-of-plane lattice parameter. The total coherency strain energy for coexistence is the composition-weighted sum of the strain energies of the terminal oxides. The coherency strain energy used in eq. (6) is the minimum value of this composition-weighted energy found across all possible coexistence directions.

The spinodal line, which dictates the metastable limit of Ge or Sn solubility, can be computed under coherent coexistence by finding the locus of points where the second derivative of the coherent disordered free energy is zero. This free energy is given by $\Delta g_{dis}^{coh} = \Delta h_{dis}^{coh}(x) - T\Delta s_{dis}(x)$, where the ideal solution entropy is used for $\Delta s_{dis}(x)$. The coherent enthalpy (eq. (6)) was fitted to a subregular solution model, and the spinodal lines for coherent phase equilibria were then computed analytically using the methodology outlined by Doak and Wolverton[49].

The coherent spinodals computed assuming coexistence

	α	β
Δe_{cs}^{001} (PBE)	0.601	-0.144
Δe_{cs}^{001} (r ² SCAN)	0.801	-0.144
Δe_{cs}^{100} (PBE)	1.176	-0.001
Δe_{cs}^{100} (r ² SCAN)	1.331	0.027
Δe_{cs}^{101} (PBE)	1.833	-0.361
Δe_{cs}^{101} (r ² SCAN)	2.108	-0.391

TABLE II. Fitting parameters for the subregular solution model of the coherency strain energy, based on eq. (2).

along the (001) plane are shown in fig. 2b. The corresponding model parameters are listed in table II. The resulting coherent spinodal, shown by the orange lines in fig. 2b, is significantly suppressed compared to the incoherent spinodal. The predicted coherent spinodal reaches a maximum temperature of 930 K (at $\approx 44\%$ Ge) with PBE and 890 K (at $\approx 65\%$ Ge) with r²SCAN. Although the incoherent mixing enthalpies are more positive with r²SCAN than with PBE, the coherent spinodal temperatures predicted by both functionals are very similar. This arises due to the stiffer elastic constants predicted by r²SCAN.

The metastable solubility limits predicted by the coherent spinodals in fig. 2 align well with recent experimental efforts to synthesize r-Sn_{1-x}Ge_xO₂. For instance, at 600 °C, the predicted coherent solubility limit of Ge ($x \approx 0.3$) closely matches the experiments by Liu *et al.*[19]. In the experiments by Takane *et al.*[15], a higher growth temperature of 725 °C was used. At this temperature, our calculations predict nearly complete solid solubility across the entire composition space, consistent with their synthesis of alloys across the full composition range.

Our computational predictions for the crystallographic parameters and finite-temperature thermodynamics of r-Sn_{1-x}Ge_xO₂ show qualitative agreement with experiments[15, 19]. The coherent spinodals predicted in fig. 2 assume that entropy arises solely from configurational disorder, that the coherency strain energy can be approximated from the strain energies of the pure phases, and that the lattice is defect-free. More rigorous estimates would require advanced techniques such as machine-learned interatomic potentials or CE models that couple ordering and strain degrees of freedom[52]. Such atomistic models would enable rigorous treatment of vibrational contributions, coherency strain energies and defects such as dislocations or semi-coherent interfaces, which have been shown to affect coherent phase separation[53–55]. Furthermore, during

thin-film growth the substrate dictates the film orientation. The actual coexistence plane and lattice parameters may differ from our estimates, yielding different metastability limits. For instance, our estimates suggest that enforcing coexistence along the (100) or (101) planes could produce complete miscibility even at low temperatures due to large coherency strain energies. If growth conditions force coexistence along these high-strain planes, interfacial defects would likely form to reduce the total free energy. Finally, our model does not account for amorphization, which has been observed experimentally. Predicting amorphization would require estimates of the amorphous phase free energy to compare against that of coherent coexistence during synthesis.

We investigated the crystallographic, electronic, and thermodynamic properties of the rutile Sn_{1-x}Ge_xO₂ alloy using density functional theory at varying levels of accuracy. Lattice parameters predicted by the PBE, r²SCAN, and HSE06 functionals agree well with experimental values and follow Vegard's law, consistent with previous reports[15, 19]. Band gap calculations using the HSE06 functional reveal strong bowing at low Ge content, also consistent with previous observations[15]. Finite-temperature phase stability calculations indicate a slightly negative SRO parameter for Ge-Sn pairs in the first neighbor shell and show that the incoherent miscibility gap cannot explain the high Ge solubilities observed in recent experiments, as it predicts low solubility at typical synthesis temperatures. Our calculations instead reveal that coherency strain suppresses the miscibility gap, enabling large Ge and Sn solubilities in agreement with experiments. These findings provide guidance for engineering UWBG semiconductors with tunable properties and highlight the role of coherency strain in enabling bandgap engineering.

YLM and ARN acknowledge funding from the NCCR MARVEL, a National Centre of Competence in Research supported by the Swiss National Science Foundation (grant 205602), which also provided hospitality and support for EK's sabbatical stay at EPFL, during which part of this work was performed. AUK, XZ, and EK were supported by the National Science Foundation through grant 2328701 which is supported in part by federal agency and industry partners through the Future of Semiconductors (FuSe) program. Computational resources were provided by Anvil at Purdue University through allocation DMR200031 from the ACCESS program, supported by U.S. National Science Foundation grants 2138259, 2138286, 2138307, 2137603, and 2138296, and by Eiger at the Swiss National Supercomputing Centre (project ID mr30) under the NCCR MARVEL allocation.

[1] M. H. Wong, O. Bierwagen, R. J. Kaplar, and H. Umezawa, Ultrawide-bandgap semiconductors: An overview, *Journal of Materials Research* **36**, 4601 (2021).

[2] J. L. Lyons and A. Janotti, A p-type dopable ultrawide-bandgap oxide, *Journal of Physics: Condensed Matter* **36**, 085501 (2023).

[3] S. Chae, N. Sanders, K. A. Mengle, A. Wang, X. Zhang, J. L. Bartolome, K. Luo, Y.-C. Huang, F. Giustino, J. T. Heron, and E. Kioupakis, Extreme-band-gap semiconductors with shallow dopants and mobile carriers (2025), arXiv:2506.07284 [cond-mat.mtrl-sci].

[4] K. A. Mengle, S. Chae, and E. Kioupakis, Quasiparticle band structure and optical properties of rutile geo2, an ultra-wide-

band-gap semiconductor, *Journal of Applied Physics* **126**, 085703 (2019).

[5] S. Chae, J. Lee, K. A. Mengle, J. T. Heron, and E. Kioupakis, Rutile geo_2 : An ultrawide-band-gap semiconductor with ambipolar doping, *Applied Physics Letters* **114**, 102104 (2019).

[6] K. Bushick, K. A. Mengle, S. Chae, and E. Kioupakis, Electron and hole mobility of rutile geo_2 from first principles: An ultrawide-bandgap semiconductor for power electronics, *Applied Physics Letters* **117**, 182104 (2020).

[7] S. Chae, K. A. Mengle, R. Lu, A. Olvera, N. Sanders, J. Lee, P. F. P. Poudeu, J. T. Heron, and E. Kioupakis, Thermal conductivity of rutile germanium dioxide, *Applied Physics Letters* **117**, 102106 (2020).

[8] S. Chae, K. Mengle, K. Bushick, J. Lee, N. Sanders, Z. Deng, Z. Mi, P. F. P. Poudeu, H. Paik, J. T. Heron, and E. Kioupakis, Toward the predictive discovery of ambipolarly dopable ultrawide-band-gap semiconductors: The case of rutile geo_2 , *Applied Physics Letters* **118**, 260501 (2021).

[9] Z. Galazka, R. Blukis, A. Fiedler, S. B. Anooz, J. Zhang, M. Albrecht, T. Remmelle, T. Schulz, D. Klimm, M. Pietsch, A. Kwasniewski, A. Dittmar, S. Ganschow, U. Juda, K. Stolze, M. Suedermann, T. Schroeder, and M. Bickermann, Bulk single crystals and physical properties of rutile geo_2 for high-power electronics and deep-ultraviolet optoelectronics, *Physica Status Solidi (B)* **262**, 2400326 (2025), published online Nov. 2024 / Aug. 2025 in print.

[10] K. Shimazoe, I. Seike, K. Kanegae, and H. Nishinaka, Enhanced growth temperature window and sb doping of rutile geo_2 enabled by graded buffer layers, *Japanese Journal of Applied Physics, Part 1: Regular Papers & Short Notes* **64**, 50903 (2025).

[11] K. Tetzner, Z. Galazka, A. Thies, A. Küberg, and O. Hilt, Lateral rutile geo_2 mosfet devices on single-crystal r- geo_2 substrates, *IEEE Electron Device Letters*, 1 (2025).

[12] K. Kanegae, K. Shimazoe, I. Seike, and H. Nishinaka, Ni/rutile geo_2 vertical schottky barrier diode on nb-doped tio_2 substrate using sb-doped graded $\text{ge}_y\text{sn}_{1-y}\text{o}_2$ buffer layers, *Applied Physics Express* **18**, 041001 (2025).

[13] Y. Nagashima, M. Fukumoto, M. Tsuchii, Y. Sugisawa, D. Sekiba, T. Hasegawa, and Y. Hirose, Deep Ultraviolet Transparent Electrode: Ta-Doped Rutile $\text{Sn}_{1-x}\text{Ge}_x\text{O}_2$, *Chemistry of Materials* **34**, 10842 (2022), publisher: American Chemical Society.

[14] E. Kluth, Y. Nagashima, S. Osawa, Y. Hirose, J. Blasing, A. Strittmatter, R. Goldhahn, and M. Feneberg, Blue shift of the absorption onset and bandgap bowing in rutile $\text{ge}_x\text{sn}_{1-x}\text{o}_2$, *Applied Physics Letters* **125**, 122102 (2024).

[15] H. Takane, Y. Ota, T. Wakamatsu, T. Araki, K. Tanaka, and K. Kaneko, Band-gap engineering of rutile-structured sno 2-geo 2-sio 2 alloy system, *Physical Review Materials* **6**, 084604 (2022), publisher: American Physical Society.

[16] A. M. Abed and R. L. Peterson, Effect of post-deposition annealing on crystal structure of rf magnetron sputtered germanium dioxide thin films, *Journal of Vacuum Science & Technology A* **42**, 063403 (2024).

[17] A. M. Abed and R. L. Peterson, Growth and characterization of rutile-type $\text{Ge}_x\text{Sn}_{1-x}\text{O}_2$ alloy thin films via rf magnetron sputtering, *APL Materials* **13**, 111115 (2025).

[18] S. Chae, H. Paik, N. M. Vu, E. Kioupakis, and J. T. Heron, Epitaxial stabilization of rutile germanium oxide thin film by molecular beam epitaxy, *Applied Physics Letters* **117**, 072105 (2020).

[19] F. Liu, N. J. Szymanski, K. Noordhoek, H.-s. Shin, D. Kim, C. J. Bartel, and B. Jalan, Unraveling the Growth Dynamics of Rutile $\text{Sn}_{1-x}\text{Ge}_x\text{O}_2$ Using Theory and Experiment, *Nano Letters* **25**, 299 (2025), publisher: American Chemical Society (ACS).

[20] J. P. Perdew, K. Burke, and M. Ernzerhof, Generalized Gradient Approximation Made Simple, *Physical Review Letters* **77**, 3865 (1996), publisher: American Physical Society.

[21] J. W. Furness, A. D. Kaplan, J. Ning, J. P. Perdew, and J. Sun, Accurate and Numerically Efficient r2SCAN Meta-Generalized Gradient Approximation, *The Journal of Physical Chemistry Letters* **10**.1021/acs.jpclett.0c02405 (2020), publisher: American Chemical Society.

[22] J. Heyd, G. E. Scuseria, and M. Ernzerhof, Hybrid functionals based on a screened Coulomb potential, *The Journal of Chemical Physics* **118**, 8207 (2003).

[23] G. Kresse and J. Furthmüller, Efficient iterative schemes for ab initio total-energy calculations using a plane-wave basis set, *Phys. Rev. B* **54**, 11169 (1996).

[24] P. E. Blöchl, Projector augmented-wave method, *Phys. Rev. B* **50**, 17953 (1994).

[25] A. Zunger, S.-H. Wei, L. G. Ferreira, and J. E. Bernard, Special quasirandom structures, *Phys. Rev. Lett.* **65**, 353 (1990).

[26] J. M. Sanchez, F. Ducastelle, and D. Gratias, Generalized cluster description of multicomponent systems, *Physica A: Statistical Mechanics and its Applications* **128**, 334 (1984).

[27] D. D. Fontaine, Cluster Approach to Order-Disorder Transformations in Alloys, in *Solid State Physics*, Vol. 47, edited by H. Ehrenreich and D. Turnbull (Academic Press, 1994) pp. 33–176.

[28] D. K. Lee, Y. L. Müller, and A. R. Natarajan, Modeling the equilibrium vacancy concentration in multi-principal element alloys from first-principles, *Acta Materialia* **304**, 121752 (2026).

[29] Y. L. Müller and A. R. Natarajan, First-principles thermodynamics of precipitation in aluminum-containing refractory alloys, *Acta Materialia* **274**, 119995 (2024).

[30] Y. L. Müller and A. R. Natarajan, Constructing multicomponent cluster expansions with machine-learning and chemical embedding, *npj Computational Materials* **11**, 60 (2025).

[31] A. R. Natarajan and A. Van der Ven, First-principles investigation of phase stability in the Mg-Sc binary alloy, *Physical Review B* **95**, 214107 (2017).

[32] A. R. Natarajan and A. Van der Ven, Machine-learning the configurational energy of multicomponent crystalline solids, *npj Computational Materials* **4**, 56 (2018).

[33] C. A. Paetsch and A. R. Natarajan, First-Principles Thermodynamics of Hydrogen Absorption in Binary C15 Laves Phases, *Chemistry of Materials* **1**, acs.chemmater.5c01925 (2026).

[34] M. Ångqvist, D. O. Lindroth, and P. Erhart, Optimization of the Thermoelectric Power Factor: Coupling between Chemical Order and Transport Properties, *Chemistry of Materials* **28**, 6877 (2016).

[35] M. Ångqvist and P. Erhart, Understanding Chemical Ordering in Intermetallic Clathrates from Atomic Scale Simulations, *Chemistry of Materials* **29**, 7554 (2017).

[36] J. Brorsson, A. E. C. Palmqvist, and P. Erhart, First-Principles Study of Order-Disorder Transitions in Pseudobinary Clathrates, *The Journal of Physical Chemistry C* **125**, 22817 (2021).

[37] D. K. J. Lee, Z. Deng, G. Sai Gautam, and P. Canepa, Thermodynamics of Sodium-Lead Alloys for Negative Electrodes from First-Principles, *Chemistry of Materials* **36**, 6831 (2024).

[38] Z. Wang, T. P. Mishra, W. Xie, Z. Deng, G. S. Gautam, A. K. Cheetham, and P. Canepa, Kinetic Monte Carlo Simulations of Sodium Ion Transport in NaSICON Electrodes, *ACS Materials Letters* **5**, 2499 (2023).

[39] S. Schulz, M. A. Caro, C. Coughlan, and E. P. O'Reilly, Composition dependent band gap and band edge bowing in alinn: A combined theoretical and experimental study, *Applied Physics Letters* **103**, 242102 (2013).

[40] M. Feneberg, C. Lidig, K. Lange, R. Goldhahn, M. D. Neumann, N. Esser, O. Bierwagen, M. E. White, M. Y. Tsai, and J. S. Speck, Ordinary and extraordinary dielectric functions of rutile SnO_2 up to 20 ev, *Applied Physics Letters* **104**, 231106 (2014).

[41] M. Stapelbroek and B. D. Evans, Exciton structure in the u.v. absorption edge of tetragonal geo_2 , *Solid State Communications* **25**, 959 (1978).

[42] A. Watanabe, T. Kikuchi, M. Tsutsumi, S. Takenouchi, and K. Uchida, Solid solubility of geo_2 in snO_2 , *Journal of the American Ceramic Society* **66**, c104 (1983).

[43] B. Puchala, J. C. Thomas, A. R. Natarajan, J. G. Goiri, S. S. Behara, J. L. Kaufman, and A. Van der Ven, CASM — A software package for first-principles based study of multicomponent crystalline solids, *Computational Materials Science* **217**, 111897 (2023).

[44] A. Van der Ven, J. Thomas, B. Puchala, and A. Natarajan, First-Principles Statistical Mechanics of Multicomponent Crystals, *Annual Review of Materials Research* **48**, 27 (2018).

[45] B. Puchala and A. Van der Ven, Thermodynamics of the $\text{Zr}-\text{O}$ system from first-principles calculations, *Physical Review B* **88**, 094108 (2013), publisher: American Physical Society.

[46] R. Tibshirani, Regression Shrinkage and Selection Via the Lasso, *Journal of the Royal Statistical Society: Series B (Methodological)* **58**, 267 (1996), _eprint: <https://onlinelibrary.wiley.com/doi/pdf/10.1111/j.2517-6161.1996.tb02080.x>.

[47] F. Pedregosa, G. Varoquaux, A. Gramfort, V. Michel, B. Thirion, O. Grisel, M. Blondel, P. Prettenhofer, R. Weiss, V. Dubourg, J. Vanderplas, A. Passos, and D. Cournapeau, Scikit-learn: Machine Learning in Python, *MACHINE LEARNING IN PYTHON*.

[48] A. R. Natarajan, E. L. Solomon, B. Puchala, E. A. Marquis, and A. Van der Ven, On the early stages of precipitation in dilute $\text{mg}-\text{nd}$ alloys, *Acta Materialia* **108**, 367 (2016).

[49] J. W. Doak and C. Wolverton, Coherent and incoherent phase stabilities of thermoelectric rocksalt IV-VI semiconductor alloys, *Physical Review B* **86**, 144202 (2012), publisher: American Physical Society.

[50] R. Malik, A. Abdellahi, and G. Ceder, A critical review of the li insertion mechanisms in lifepo_4 electrodes, *Journal of The Electrochemical Society* **160**, A3179 (2013).

[51] J. W. Cahn, On spinodal decomposition, *Acta Metallurgica* **9**, 795 (1961).

[52] S. S. Behara, J. C. Thomas, B. Puchala, and A. Van der Ven, Chemomechanics in alloy phase stability, *Phys. Rev. Mater.* **8**, 033801 (2024).

[53] F. m. c. Léonard and R. C. Desai, Spinodal decomposition and dislocation lines in thin films and bulk materials, *Phys. Rev. B* **58**, 8277 (1998).

[54] S. Hu and L. Chen, Solute segregation and coherent nucleation and growth near a dislocation—a phase-field model integrating defect and phase microstructures, *Acta Materialia* **49**, 463 (2001).

[55] S. Hu and L. Chen, Diffuse-interface modeling of composition evolution in the presence of structural defects, *Computational Materials Science* **23**, 270 (2002).